

# Shallow crustal structures of the Indian ocean derived from compliance function analysis

Mohammad Amin Aminian<sup>1</sup>,<sup>1</sup> Wayne Crawford,<sup>1</sup> Éléonore Stutzmann,<sup>1</sup> Jean-Paul Montagner,<sup>1</sup> Mathilde Cannat<sup>1</sup> and Céline Hadziioannou<sup>1,2</sup>

<sup>1</sup>*Institut de Physique du Globe de Paris, Université Paris Cité, 75005 Paris, France. E-mail: [Aminian@ipgp.com](mailto:Aminian@ipgp.com)*

<sup>2</sup>*Institute of Geophysics, Centre for Earth System Research and Sustainability, University of Hamburg, 20146 Hamburg, Germany*

Accepted 2025 June 24. Received 2025 June 12; in original form 2024 August 28

## SUMMARY

We used broad-band ocean bottom seismometer data from the RHUM-RUM (Réunion Hotspot and Upper Mantle - Réunions Unterer Mantel) experiment to derive the compliance function and estimate the shear velocity ( $V_s$ ) structure of the subsurface at several sites beneath the Indian Ocean. The primary objective is to map the geological features of poorly explored marine regions, utilizing the compliance function, a measure of seafloor deformation in response to infragravity pressure signals at low frequencies (0.003 to 0.04 Hz). Compliance is the transfer function between vertical displacement and pressure, which is most sensitive to subsurface shear velocities. Our analytical process involves several data processing steps, including the removal of glitches, filtering out seismic events, minimizing tilt effects, calibrating pressure gauges, searching over the frequency and coherence domains to determine the optimal data window and performing depth-velocity inversion using Monte Carlo method, specifically the Metropolis–Hastings algorithm. We present the ‘ComPy’ software, which automates these processing steps for seafloor compliance analysis. The data, recorded over 13 months in 2012–2013 over a large region stretching from La Reunion Island to the Central Indian Ridge and the South–West Indian Ridge (SWIR) (water depths of 3 to 5 km), confirm the stability of the compliance function over time. Depth-velocity inversions of the derived compliance measurements, using the Metropolis–Hastings algorithm, illuminate the  $V_s$  structure of the oceanic crust down to 8 km. Low  $V_s$  anomalies in the crust at the SWIR are consistent with significant serpentinization of a crustal component of tectonically exhumed mantle-derived peridotites.

**Key words:** Oceanic crust; Inversion; Indian Ocean; Monte Carlo methods; Crustal imaging; Mid-Ocean ridge processes..

## 1 INTRODUCTION

Oceanic crust formation at mid-ocean ridges arises from the interplay of tectonism, magmatism and hydrothermal alteration, with spreading rate and mantle conditions governing distinct crustal characteristics. This study focuses on a geologically diverse region of the Indian Ocean, encompassing the oceanic Somali Plate and three major mid-ocean ridges: the Central Indian Ridge (CIR; spatial extent: 25°S to 1°S, 65°E to 70°E), the Southwest Indian Ridge (SWIR; 25°S to 55°S, 0°E to 70°E), and the Southeast Indian Ridge (SEIR; 25°S to 60°S, 70°E to 160°E), which converge at the Rodrigues Triple Junction (RTJ; 25°S, 70°E). The Somali Plate exhibits variable sedimentation and lithification patterns, shaped by complex tectono-sedimentary processes. The region features an intermediate-spreading ridge (CIR,  $\sim 30$ – $49$  mm yr<sup>-1</sup>; e.g. Krishna 1996; Drolia *et al.* 2000; Kamesh Raju *et al.* 2012) and an ultraslow spreading ridge (SWIR,  $\sim 13$ – $16$  mm yr<sup>-1</sup>; e.g. Patriat & Segoufin

1988; Cannat *et al.* 1999). The evolution of the RTJ reflects major reorganizations in Indian Ocean spreading systems since the Late Cretaceous, including changes in ridge segmentation and asymmetric spreading (Müller *et al.* 2008). This first-order tectonic boundary, shaped by divergent plate motions and variable spreading rates, gives rise to significant variations in crustal and upper mantle structure. This geodynamic diversity provides a rare natural laboratory to investigate active processes such as serpentinization and magmatism, which are central to lithospheric formation and hydrothermal alteration.

Our investigation, based on the analysis of oceanic crust structure, leverages data from several isolated ocean-bottom seismometer stations. This approach demonstrates how high-resolution local measurements can be used to explore and illuminate large-scale geodynamic phenomena. Spreading regimes, thermal gradients, and tectonic processes collectively shape oceanic crustal structure and evolution (Searle 2013). One method for probing crustal structure is

through the analysis of seismic shear wave velocity models. These models make it possible to assess crustal lithology, fluid content, sediment characteristics and temporal evolution. One difficulty in obtaining such models is that accurate measurements of shear waves at the ocean bottom pose significant technical and scientific challenges, due to the difficulty of artificially generating shear waves beneath the ocean. (e.g. Hulme *et al.* 2003; Crawford & Singh 2008; Ruan *et al.* 2014). The seafloor compliance is a measure of the seafloor response to the pressure created by oceanic infragravity surface waves. Compliance is an effective technique for constraining the shear velocity ( $V_s$ ) of the oceanic crust (Bradner 1963; Yamamoto & Torii 1986), and particularly low shear velocity regions associated with fluids or fluid-based alteration Crawford (2004). Compliance measurements require simultaneous and well-calibrated seismological and pressure measurements in the frequency band from 0.003 to 0.1 Hz (Crawford *et al.* 1991).

Subsurface  $V_s$  values are estimated from compliance measurements using geophysical data inversion (Crawford *et al.* 1991). This method has proven especially valuable in regions with low-velocity anomalies, which are challenging to image using active seismic methods (e.g. Yamamoto & Torii 1986; Crawford & Singh 2008; Ruan *et al.* 2014). The method can be used to estimate subsurface structure and the existence of low-velocity anomalies in poorly explored areas, including single-site measurements. In this case, compliance can be used to construct a 1-D  $V_s$  model that represents the average structure over a horizontal extent similar to the depth in the model (Crawford *et al.* 1998). Compliance at deep-ocean sites (>1500 m water depth) is generally sensitive to the first 6–10 km of subsurface structure (Crawford *et al.* 1998).

Seafloor compliance studies have provided new insights into various aspects of oceanic crustal geology, ranging from the behaviour of gas hydrates to the dynamics of magmatic systems (Willoughby & Edwards 1997; Crawford *et al.* 1998). Recent studies have highlighted the use of seafloor compliance measurements to advance our understanding of faulting and hydration of oceanic upper crust generated by continental rifting (Kuo *et al.* 2015) and the distribution of magma beneath oceanic spreading centres (Crawford & Webb 2002; Doran & Crawford 2020).

Wang *et al.* (2010) demonstrated that the quality of seafloor compliance measurement is significantly influenced by sea state conditions, with high-coherence data favoured by shallow waters and rough seas. Recent advances in compliance measurements include the first consistent observations of horizontal seafloor compliance induced by infragravity waves, whose generation is primarily confined to the near-coastal environment (Doran & Laske 2016).

Methodologies developed to minimize tilt effects in ocean bottom seismic records (e.g. Crawford & Webb 2000; Bell *et al.* 2015; Tian & Ritzwoller 2017; Janiszewski *et al.* 2019; Harmon *et al.* 2022), have further improved our ability to measure seafloor compliance. These techniques have played a crucial role in minimizing the impact of different types of noises on the vertical channel, improving seismic signal detection and enabling more precise compliance measurement. Despite these advancements, there is still a need for improved methodologies to increase the accuracy of seafloor compliance measurements and to estimate high-resolution  $V_s$  models from measured compliances.

We present here a new consistent compliance measurement and inversion methodology, taking into account recent developments in glitch removal (Deen *et al.* 2017), tilt reduction (Janiszewski *et al.* 2019; Harmon *et al.* 2022) and inversion (Zha & Webb 2016; Mosher *et al.* 2021b). We also designed a new approach to invert the compliance function for depth structure, which significantly

increases the accuracy and resolution of the resulting  $V_s$  model, offering an enhanced level of detail for understanding subsurface dynamics. This technique is based on Monte Carlo inversion, enhanced by introducing constraints based on fractions of prior models and the lithological and tectonic characteristics of the ocean floor, such as sediment layers with varying degrees of consolidation or serpentinized peridotites with different degrees of alteration, as well as the approximate depth of the Moho. Although Monte Carlo can explore a wide range of models, our approach refines this exploration to enhance efficiency and accuracy by incorporating adaptive step sizes and measurement uncertainties into the cost function, which accounts for discrepancies between measured and theoretical uncertainties, improving the search efficiency of the inversion process. The ability to incorporate measurement uncertainties into the inversion process and to provide uncertainty estimates for the inverted model are additional advantages of the Markov Chain Monte Carlo (MCMC) method. Furthermore, including prior constraints is a pragmatic strategy, as these constraints help ensure that the resulting model is physically realistic.

We use data from the RHUM-RUM experiment (Barruol & Sigloch 2013), which recorded high-quality seismic and pressure data for more than one year at several broad-band ocean bottom seismometer (BBOBS) stations in the Indian ocean, in various tectonic contexts (Fig. 1). Using measured compliances, we estimate 1-D  $V_s$  models of the oceanic subsurface, using a Monte Carlo inversion (Mosegaard & Tarantola 1995). The different crustal models obtained in these different tectonic contexts (off-axis oceanic crust, mid-ocean ridge crust formed at an ultraslow and at an intermediate spreading ridge) are a first step towards investigating the dynamic evolution of the oceanic crust beneath the Indian Ocean.

## 2 THEORY

### 2.1 Seafloor compliance

The vertical seafloor compliance,  $\zeta(\omega)$ , as a function of angular frequency  $\omega$ , is defined as the ratio between the spectra of the vertical displacement,  $u_z(\omega)$ , and the vertical stress,  $\tau_{zz}(\omega)$ , at the seafloor (Sorrells & Goforth 1973):

$$\zeta(\omega) = \frac{u_z}{\tau_{zz}}(\omega) \quad (1)$$

Vertical ground displacement and stress at the ocean bottom are due to passing free infragravity waves (e.g. Bertin *et al.* 2018). Free infragravity waves are generated by the grouping of shorter ocean surface waves, followed by shoaling and reflection at an ocean–land boundary. They have low frequencies ranging from 0.005 to 0.05 Hz and penetrate down to the ocean floor (Herbers *et al.* 1994; Rawat *et al.* 2014).

Their wavenumber  $k(\omega)$  is computed using the linear ocean surface gravity wave dispersion relation:

$$\omega^2 = gk(\omega) \tanh(k(\omega)H), \quad (2)$$

where  $\omega$  is the angular frequency,  $g$  is the acceleration of the earth's gravity and  $H$  is the ocean thickness. We approximate the tanh function as proposed by Mosher *et al.* (2021a):

$$\tanh(x) \equiv \begin{cases} \frac{x(27+x^2)}{27+9x^2} & \text{if } 0 \leq x < 2.96 \\ 1 & \text{if } x \geq 2.96 \end{cases}, \quad (3)$$

which uses a quartic equation for  $x$ , guaranteeing stability at the cost of up to 2 per cent error. Sorrells & Goforth (1973) first computed

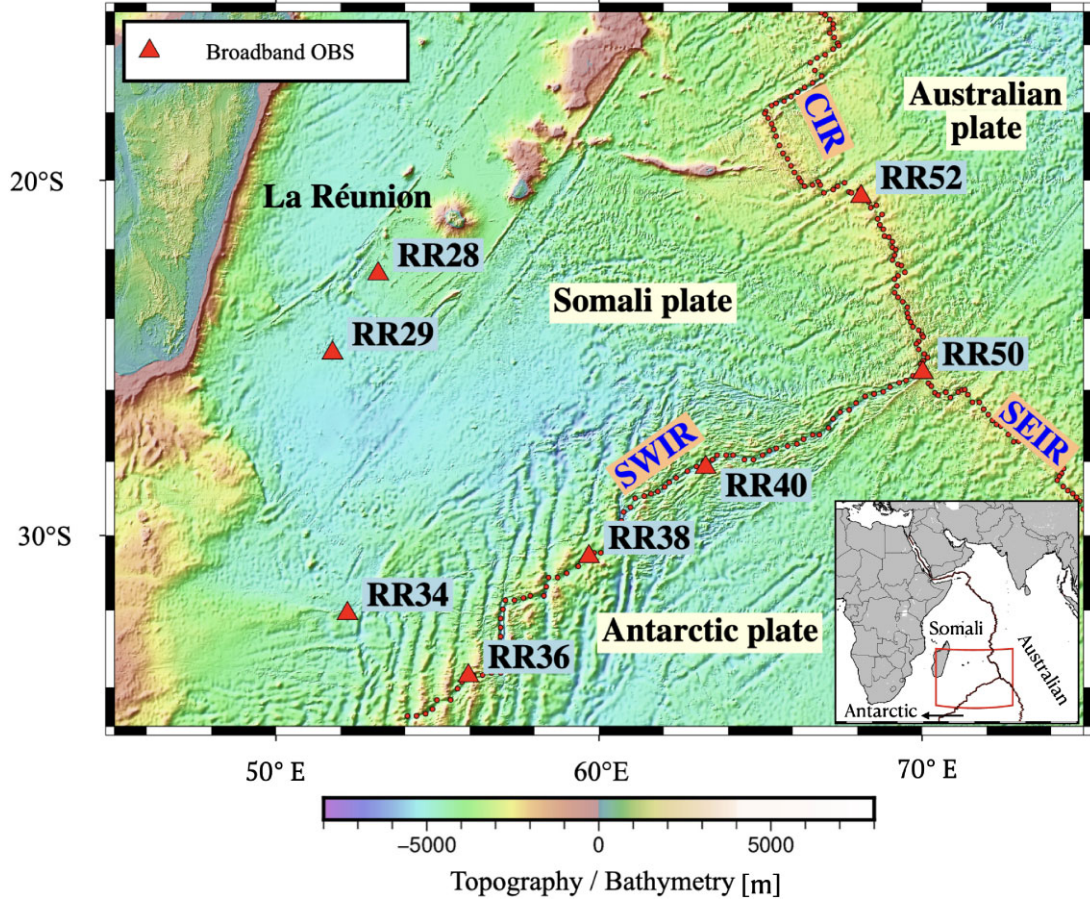


**Figure 1.** Overview map of the RHUM-RUM experiment's BBOBS used in this study (triangles labelled with station names), superimposed on seafloor bathymetry. Dotted lines indicate the ridge axis (SWIR: South-West Indian Ridge; CIR: Central Indian Ridge; SEIR: South-East Indian Ridge). The inset map shows the location of the experiment area, delineated by a box.

the compliance for a uniform half-space:

$$\zeta(\omega) = -\frac{1}{k(\omega)} \left[ \frac{\lambda + 2\mu}{2\mu(\lambda + \mu)} \right] \quad (4)$$

where  $\lambda$  is the Lamé parameter related to the material's compressibility, and  $\mu$  is the shear modulus that measures the resistance to shear deformation. This ratio is affected by the characteristics of the seabed material, primarily its stiffness, which refers to the material's overall resistance to deformation under applied forces. Given that  $\lambda$ , and  $\mu$  are positive values, it follows that all the corresponding partial derivatives with respect to the Lamé parameters are negative. This implies that any increase in the values of the Lamé parameters will lead to a reduction in the vertical compliance magnitude (Crawford *et al.* 1991). The compliance function is more sensitive to variations in  $\mu$  than to changes in  $\lambda$ . This sensitivity makes it effective for detecting material's shear strength/velocity variations.

In a more realistic 1-D layered Earth model, the vertical compliance defined by eq. (1) is computed numerically using the matrix-propagator method (Kennett 2009). We use an implementation of the minor vector propagator written by Gombert & Masters (1988). Henceforth, whenever we mention compliance, we implicitly mean normalized vertical compliance,  $\hat{\eta}(\omega)$ , which is obtained by multiplying the compliance by the wavenumber of infragravity waves, to remove the masking effect of the ocean water depth.

$$\eta(\omega) = k(\omega)\zeta(\omega) \quad (5)$$

## 2.2 Compliance measurements

The measured compliance, denoted as  $\hat{\eta}(\omega)$ , is computed as follows:

$$\hat{\eta}(\omega) = k(\omega)\hat{\gamma}_{pz}(\omega)\sqrt{\frac{\hat{S}_z(\omega)}{\hat{S}_p(\omega)}}, \quad (6)$$

where  $\hat{S}_z(\omega)$  and  $\hat{S}_p(\omega)$  are the power spectral density of the measured vertical displacement and pressure respectively. Their coherence,  $\hat{\gamma}_{pz}(\omega)$ , is defined as:

$$\hat{\gamma}_{pz}(\omega) = \sqrt{\frac{|\hat{C}_{pz}(\omega)|^2}{\hat{S}_p(\omega)\hat{S}_z(\omega)}}, \quad (7)$$

where  $\hat{C}_{pz}(\omega)$  is the cross-power spectral density between measured pressure and vertical displacement. We calculate  $\hat{S}_z(\omega)$  and  $\hat{S}_p(\omega)$  and  $\hat{C}_{pz}(\omega)$  using Welch's method (Welch 1967). The inclusion of coherence in eq. (6) removes the effect of non-pressure sources of displacement at the seafloor, assuming that all other noise is on the seismometer channel (Crawford *et al.* 1991).

We estimate the uncertainty  $\epsilon$  of the measured compliance as follows (Bendat & Piersol 1993):

$$\epsilon[|\hat{\eta}(\omega)|] = \frac{\sqrt{1 - \hat{\gamma}_{pz}^2(\omega)}}{|\hat{\gamma}_{pz}(\omega)|\sqrt{2n_d}}|\hat{\eta}(\omega)| \quad (8)$$

with  $n_d$  the number of data windows used to calculate the coherence function and spectra. In this study, we used more than 500 time windows per station. Compliance calculations followed the method of Rebeyrol *et al.* (2024), using a 0.005 Hz resolution in the infragravity wave range.

### 3 DATA SET

The RHUM-RUM experiment (Barruol & Sigloch 2013), conducted from November 2012 to October 2013, is designed to investigate the Indian Ocean near La Réunion Island. This ambitious study deployed 57 Ocean Bottom Seismometers (OBS) across a sprawling area exceeding 4 million square kilometers, gathering seismological data in a region marked by complex geological features.

Nine of the broad-band stations were equipped with Nanometrics Trillium 240 seismometers and differential pressure gauges, capable of measuring seafloor compliance. These stations recorded at a sampling rate of 62.5 Hz and obtained the best sensitivity of all stations for periods longer than 10 s (Stähler *et al.* 2016). One of these stations had a noisy pressure channel, so we analysed compliance for the remaining eight. The differential pressure gauges (Cox *et al.* 1984) record pressure fluctuations efficiently in the 0.002–30 Hz frequency range. Selecting highly sensitive sensors with a wide frequency range is crucial for obtaining high-resolution seafloor compliance measurements.

Fig. 1 presents the location of these BBOBSs, the seafloor bathymetry, and major structures. The water depth ranges from 2918 to 4829 m over these stations. The distribution of these stations spans a diversity of geodynamic settings:

- Mid-ocean ridges (on or near the spreading ridge axes); intermediate spreading CIR with a spreading rate of 23 mm yr<sup>-1</sup> at station RR52; ultraslow spreading SWIR with a spreading rate of 14 mm yr<sup>-1</sup> at stations RR36, RR38 and RR40; RTJ at station RR50. A high-resolution bathymetric grid map displaying stations on the mid-ocean ridge is provided in the Supporting Information, Fig. S2, which includes cross-sections both orthogonal to and along the ridge axes, as well as the specific locations of the stations.
- Intra-oceanic Somali plate; RR28 situated on a 64.5-million-year-old lithosphere 300 km away from the La Réunion hotspot, overlain by a 145 m sedimentary layer; RR29 on a 70-million-year-old lithosphere 500 km distant from the La Réunion hotspot, with a sedimentary cover of 110 m; and RR34 located on a 57-million-year-old lithosphere 1250 km from the La Réunion hotspot, capped by a 400 m sedimentary layer, offering a diverse range of data points for analysis. The age of the plate and thickness of the sedimentary layers are from Müller *et al.* (2008) and Straume *et al.* (2019).

### 4 DATA PROCESSING, COMPLIANCE MEASUREMENT AND SHEAR VELOCITY INVERSION

The recorded data at the ocean bottom are contaminated by various types of events and noise, such as local and global earthquakes, periodic transient noise and tilt, making it challenging to measure the compliance. To remove or minimize these undesired signals, we pre-processed the data and chose best-quality time windows for analysis as explained below. Fig. 2 presents the full processing flowchart, encompassing data pre-processing and the main process, essential for estimating the  $V_s$  model beneath the OBS. In the following sections, we present a detailed analysis of one year of data from station RR52, located on the CIR. Data processing for the other stations is illustrated in Fig. S3 (Supporting Information).

Our focus is to demonstrate the influence of pre-processing and processing stages on seismic and pressure data, ultimately aiding in the computation of a compliance function with reduced bias within the compliance frequency band.

Fig. 3 shows power spectral density (PSDs) of the vertical seismological channel at different pre-processing stages. Although we use the seafloor displacement to calculate compliance, we show the corresponding PSDs with respect to acceleration in order to facilitate comparison with standard seismological noise spectra. We calculated the PSDs using Welch's method (Welch 1967), eliminating time windows in which any seismometer component is saturated and unusable, then removing the instrument response. These processes collectively reduce the noise level on the vertical channel by 20 dB within the compliance frequency band (infragravity frequencies), leading to the emergence of the characteristic compliance peak approximately centred at 0.01 Hz. This reduction unveils the compliance effect on the PSD, seen as a distinct bump around 0.01 Hz, highlighted in pale green in Fig. 3. To better reveal this effect, we also plot the PSD with the compliance signal removed using the generalized method of Webb & Crawford (1999).

#### 4.1 Data pre-processing

##### 4.1.1 Tilt reduction

If the seismometer's vertical channel is misoriented from the gravitational field, tilting caused by ocean bottom currents, which primarily affects the horizontal channels, leaks onto the vertical record (Bell *et al.* 2015). The seismometer may be misaligned with the gravitational field because of imperfect calibration or precision of the leveling system: subsequent drift from this initial alignment is primarily attributed to the seismometer's settling (Tolstoy *et al.* 1998). To minimize this effect, we use hourly synthetic rotation corrections to realign the seismometer's vertical channel with the gravitational field.

We use the same methodology as Harmon *et al.* (2022) to identify the optimal tilt rotation angles, by minimizing the variance of the rotated vertical component, without needing to know the instrument's horizontal geographic orientation. By converting  $h_1(t)$  and  $h_2(t)$ , two horizontal channels, into a radial components along the tilt direction and a transverse component, the tilt correction is optimized. A subsequent rotation between the vertical and radial components reduces the noise energy of the rotated vertical component. After determining the optimal angles, we apply the rotation to the raw data to achieve tilt-corrected data.

Fig. 4 illustrates hourly measurements of azimuth and incident angles for station RR52 over the period from 2012 October 20 to 2013 October 11 (hourly measurements for the other stations are illustrated in Figs 4 and 5). The incident angle is a measure of the seismometer's tilt away from the vertical axis, while the azimuth is an indication of the tilt direction relative to one channel's positive axis, identified here as  $h_1$ . The colour intensity of each data point represents the common logarithm (base 10) of variance reduction, with darker colours indicating higher variance reduction, and lighter colours indicating lower variance reduction.

The azimuth and incident angles both increase over the first seven months after the deployment of the seismometer (Fig. 4). This progressive increase was followed by a jump on 2013 May 2 and then a gradual stabilization. We attribute the stabilization to the seismometer settling onto the ocean floor. By the end of the deployment, the seismometer had almost completely settled, as evidenced by the flattening of the azimuth and incident angle curves.

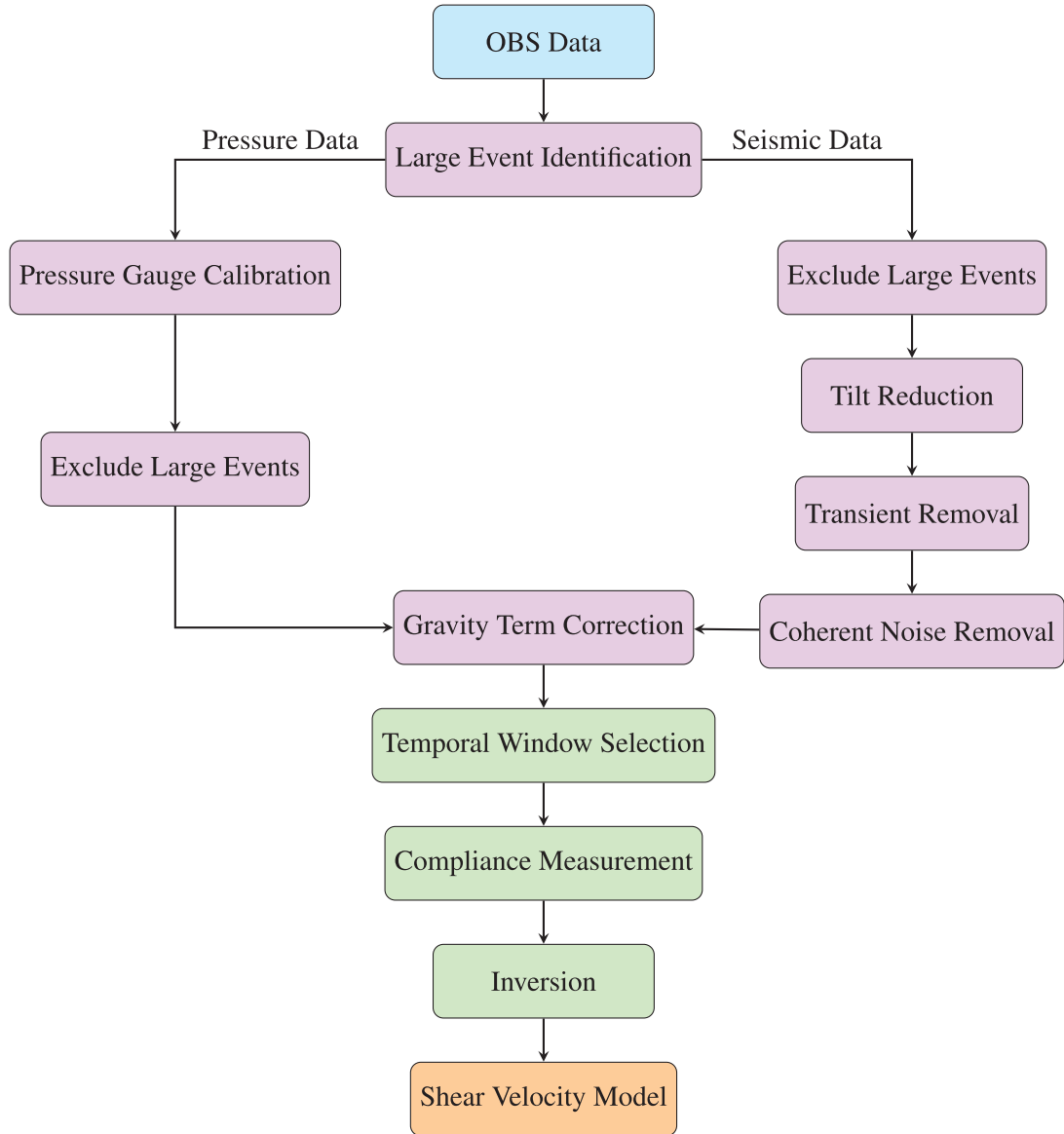


**Figure 2.** Flowchart illustrating the data pre-processing and main processes for estimating the shear velocity ( $V_s$ ) model beneath the OBS.

#### 4.1.2 Identification of global earthquakes and local events

In the next stage, we mitigate the impact of global and local seismic events. These events have a different pressure-acceleration relation than does seafloor compliance, so they could generate a strong coherence but an inconsistent transfer function (Doran & Laske 2016).

To identify global seismic events, we use the United States Geological Survey (USGS) catalogue of earthquakes with a magnitude ( $M_w$ ) exceeding 5.5. Following the methodology described in Deen *et al.* (2017), we exclude time periods for earthquakes exceeding a magnitude of 6 according to the equation  $T_{\text{exclude}} = (M_w - 5.85) * 36$  hr. For example, 5.4 hr of data will be excluded after a magnitude 6 earthquake and 41.4 hr will be excluded after a magnitude 7 event.

To identify local events such as earthquakes, we employed the methodology described in Withers *et al.* (1998), consisting of a recursive STA/LTA trigger to estimate  $P$ -wave arrival times, after which we remove the events from the data. For earthquakes, we removed data corresponding to the duration of the  $P$ -wave and sub-

sequent seismic phases, typically spanning several minutes based on the event's characteristics and arrival time patterns.

#### 4.1.3 Transient glitch removal

The BBOBS whose data we use are affected by a periodic transient, induced about every hour by a serial interrogation of the seismometer's mass centre positions. These transients induce up to 20 min of noise at each occurrence and significantly contaminate the signal across a broad and extended frequency range.

To mitigate this specific noise, we followed the method of Deen *et al.* (2017). First, the data are segmented into intervals corresponding to the glitch periodicity. Subsequently, the aligned data segments are stacked to obtain the average glitch and this average glitch is then convolved with a comb function to generate a synthetic transient-only signal, which is subtracted from the real data. The average glitch is valuable for identifying and subsequently eliminating any residuals from the steepest section of the pulse. To achieve this, each glitch present in the data is fitted with a sum of one left-shifted

## YV.RR52 2012-10-20--2013-09-15 [Hourly]

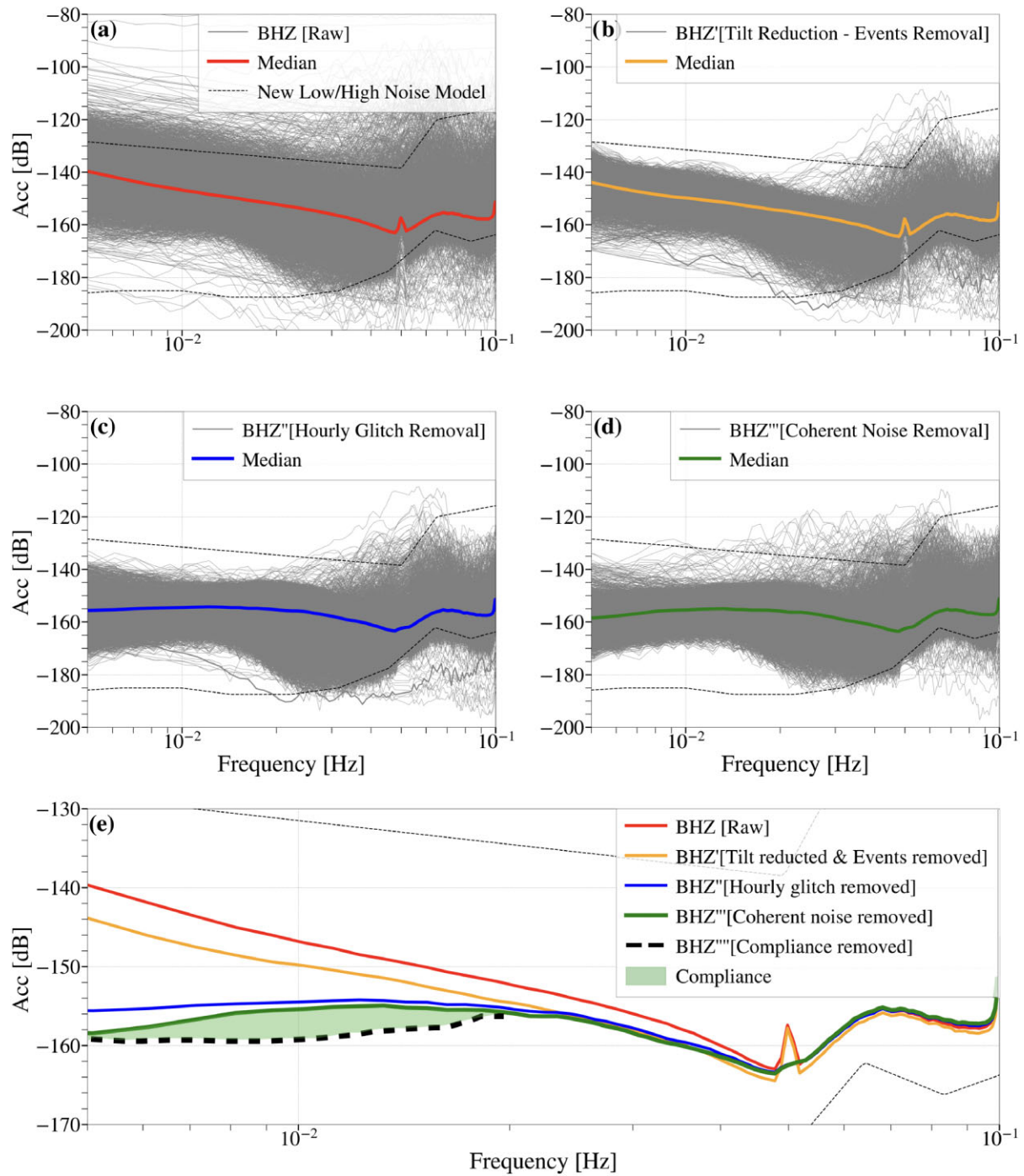


**Figure 3.** Vertical channel PSDs for different stages of seismic data preprocessing at station RR52. (a) the raw data ( $BHZ$ ); (b) after tilt correction and removal of local and global events ( $BHZ'$ ); (c) after transient noise (glitch) elimination ( $BHZ''$ ); (d) after removing coherent noise using the transfer function method ( $BHZ'''$ ); (e) comparison of median PSDs for each stage, highlighting the compliance bump, ( $BHZ''''$ ) shows the data after removing compliance.

and one right-shifted average pulse. This fitting process involves two free parameters, which correspond to adjusting the amplitude and the position of the glitch within a range of plus or minus one sampling interval. By accurately fitting these shifted average pulses to the glitches, we effectively remove the glitches from the data. More details and the effect of this stage on the vertical seismic data are provided in Fig. S1 (Supporting Information).

#### 4.1.4 Coherent noise removal

To remove the coherent noise, primarily the residual tilt effect, from the vertical channel, we employ a modified version of the transfer function method described by Crawford & Webb (2000). This involves removing the coherent energy of the horizontal channels from the vertical channel in frequency domain.

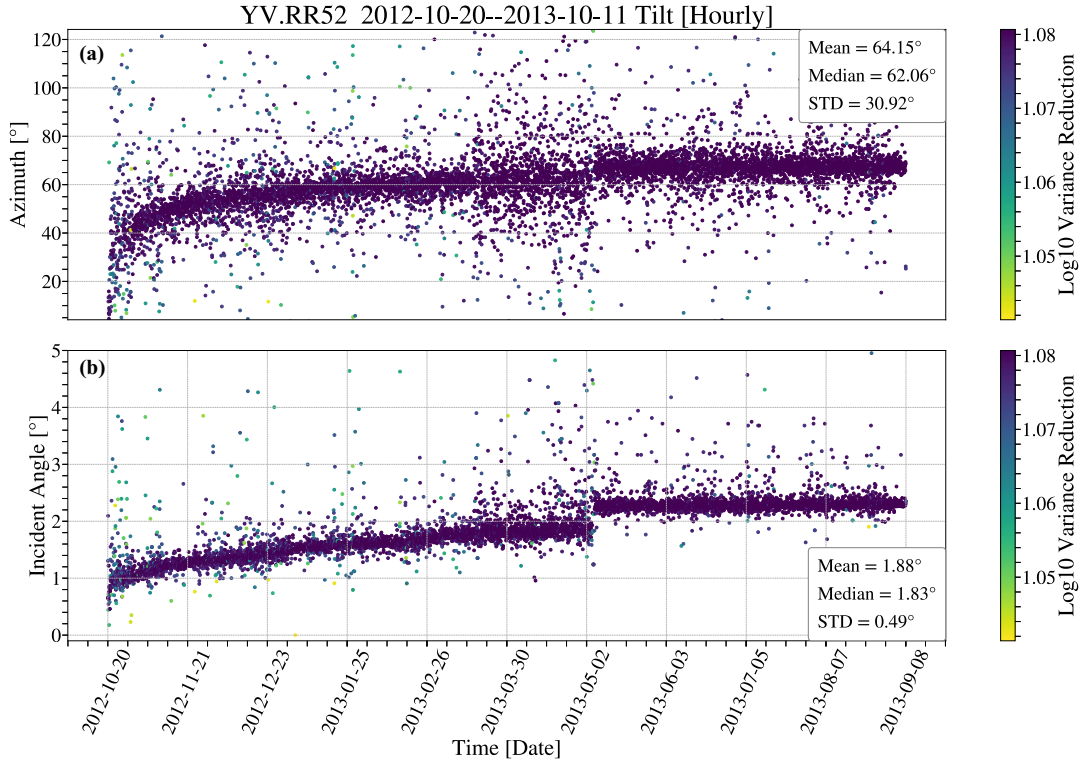


**Figure 4.** Hourly tilt azimuth and incident angles minimizing variance on the vertical channel, for one year at station RR52.

To implement this method, we segment data into sub-windows (varying between 12 and 24 hr depending on data quality), then compute coherence functions  $\hat{\gamma}_{zh_1}$ ,  $\hat{\gamma}_{zh_2}$  between the horizontal channels ( $\hat{h}_1(t)$  and  $\hat{h}_2(t)$ ) and the vertical channel for each segment using eq. (7).

We first remove the coherent energy of the dominant horizontal channel,  $\hat{h}_{\text{Dominant}}(t)$ , with higher coherency with the vertical channel, from the vertical channel before addressing the weaker horizontal channel, which corresponds to the one with lower coherency.

The transfer function between the vertical and the horizontal channels,  $\hat{T}_{zh}(\omega)$  is:

$$\hat{T}_{zh}(\omega) = \sqrt{\frac{\hat{S}_z(\omega)}{\hat{S}_h(\omega)}} \quad (9)$$

To remove coherent tilt noise from the horizontal channel of the vertical channel, we use the following equation:

$$\hat{S}_{z'}(\omega) = \hat{S}_z(\omega) - \hat{\gamma}_{zh}(\omega) \cdot \hat{T}_{zh}(\omega) \quad (10)$$

where  $\hat{S}_{z'}$  is the corrected vertical channel from the initial or dominant horizontal channel. To eliminate the energy contribution of the second horizontal channel from the corrected vertical channel ( $\hat{S}_{z'}$ ), we use eq. (10) for the second horizontal channel. This time, we treat the second horizontal as the dominant horizontal, and instead of  $\hat{S}_z$ , we use  $\hat{S}_{z'}$  in eq. (10), eq. (9) and eq. (7).

We perform the tilt correction in two steps because the first rotation step (Section 4.1.1) enhances the removal of glitches by preserving the waveform, thus ensuring that the stacking of glitches is performed on non-deformed data. During the second tilt correction using the transfer function method (this section), the remaining coherent energy with horizontal channels in the frequency band of interest are eliminated from the vertical channel.

#### 4.1.5 Pressure gauge calibration

It is difficult and perhaps futile to calibrate differential pressure gauge (DPG) in the laboratory, because their response depends on the compressibility and viscosity of the gauge's oil, which in turn depends on the seafloor temperature and pressure (Doran *et al.* 2019). To calibrate the DPG *in situ*, we specifically utilized the measured and theoretical pressure-acceleration transfer function, following the methodology described by Zha & Webb (2016) and Ruan *et al.* (2014). This involves fitting, for teleseismic events with  $M_w > 7$ , the measured spectral ratio of Rayleigh waves between the pressure and vertical channels to the theoretical spectral ratio. To accurately detect the arrival times of teleseismic Rayleigh waves, we employ PhaseNet (Zhu & Beroza 2019), a deep-neural-network-based arrival-time picking method, followed by an analysis of amplitude variations after *P*- and *S*-wave arrivals to estimate Rayleigh wave arrivals.

Fig. 5(a) illustrates the coherence function between pressure and vertical acceleration induced by teleseismic large earthquakes. By applying a median filter in the frequency-coherence domain, specifically targeting the Rayleigh wave frequency band, we can identify and use events with high coherence (close to 1) within the Rayleigh wave frequency band, thereby reducing bias in our calculations; Fig. 5(b) displays the normalized spectral ratio (divided by water weight,  $\rho h$ ) of high-coherence teleseismic large events. We computed the gain factors by implementing a grid search method to align the theoretical pressure-acceleration ( $p/a$ ) spectral ratio with each measured ratio (green lines) multiplied by the gain factor.

The DPG gain factors in this study range from 0.6 to 0.8 and do not change over time. Table 1 presents the gain factor associated with each OBS, along with the OBS locations and frequency band limits that we will use in the next section for the compliance measurements.

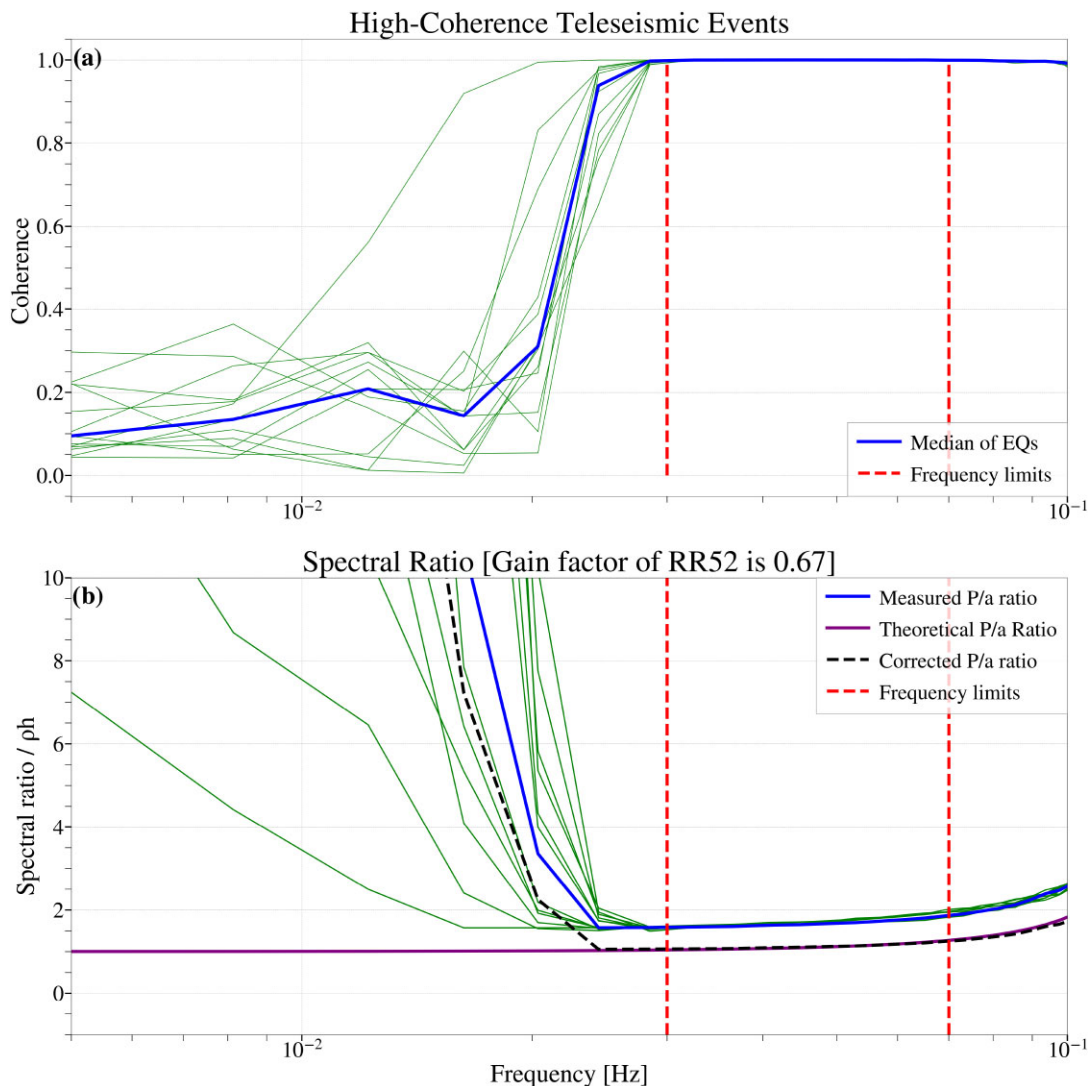


**Figure 5.** (a) Coherence between pressure and vertical acceleration in response to teleseismic earthquakes at Station RR52, for selected events having high coherence. The median coherence is shown, with the vertical dashed lines marking the boundaries of the Rayleigh wave frequency band used in this method. (b) Normalized spectral ratios for these events, showing the alignment of theoretical ratio with observed ratios. The corrected spectral ratio, achieved by multiplying the observed ratio with the optimal gain factor, is shown in dashed line.

**Table 1.** Table of Station Information, which includes gain factors calculated using data from at least seven large teleseismic earthquakes per station, along with geospatial data from other studies.

Station	Latitude [°]	Longitude [°]	Depth [m]	Gain Factor	Frequency* [Hz]
RR28	-22.7152	53.1595	4550	$0.78 \pm 0.039$	0.0066–0.0162
RR29	-24.9657	51.7488	4829	$0.70 \pm 0.035$	0.0061–0.0147
RR34	-32.0783	52.2114	4265	$0.58 \pm 0.029$	0.0071–0.0152
RR36	-33.7018	55.9578	3560	$0.64 \pm 0.032$	0.0076–0.0188
RR38	-30.5650	59.6858	4560	$0.60 \pm 0.030$	0.0066–0.0162
RR40	-28.1461	63.3020	4780	$0.74 \pm 0.037$	0.0081–0.0157
RR50	-25.5182	70.0222	4118	$0.68 \pm 0.034$	0.0071–0.0152
RR52	-20.4723	68.1094	2918	$0.67 \pm 0.034$	0.0071–0.0193

Frequency\* = Frequency Limits of Compliance Function.

We incorporate the measured pressure gain factor into our Shear Velocity Inversion (Section 4.3), allowing the gain factor to vary by a maximum of 5 per cent (standard deviations of gain factor results) from its initial value (average of the resulting factors) to account for uncertainty. As shown in the table, this uncertainty is about 5 per cent. By adding this to compliance uncertainty, we achieve a more reliable estimate of the output model uncertainty.

#### 4.1.6 Gravity term correction

Seafloor vertical acceleration measurements are not only sensitive to the desired ground motion  $a_d$ , but also to the gravitational attraction of the ocean waves,  $a_w$ , and the change in distance from the earth's centre of mass,  $a_e$  (Crawford *et al.* 1998). For seafloor depths between 2.9 and 4.8 km, compliance is measured in the frequency band from approximately 0.006 to 0.019 Hz. In this band,  $a_d$

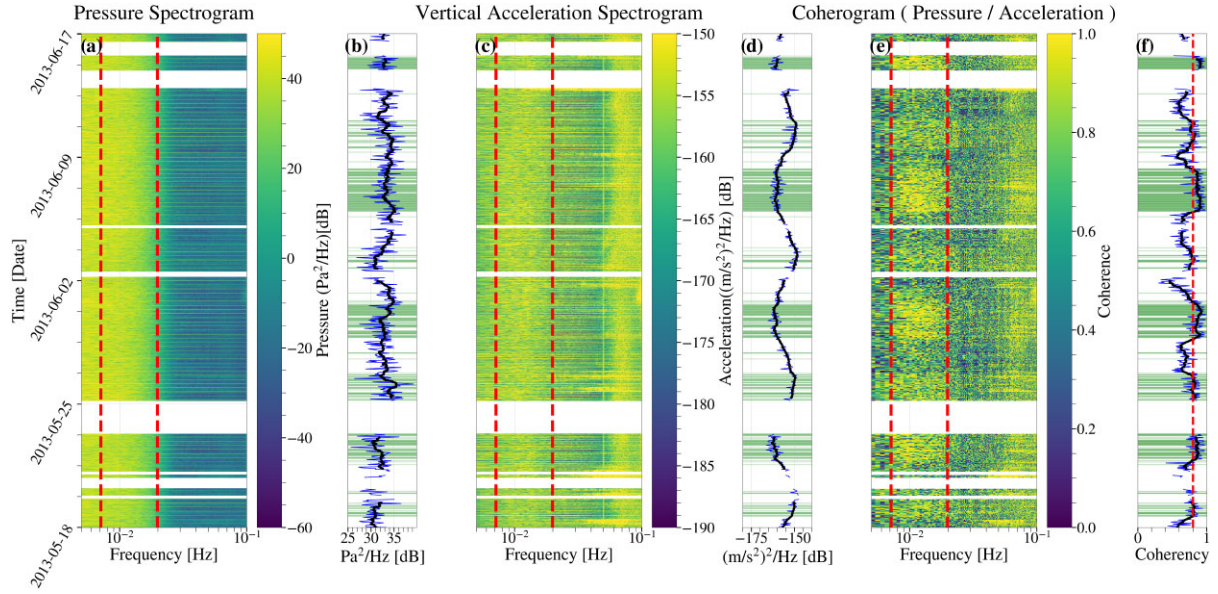


**Figure 6.** Spectrograms of station RR52 over a one-month period, featuring average values within the compliance frequency band, include: (a) calibrated pressure, (b) its median values and the smoothed values of the median, (c) corrected vertical acceleration, (d) its median values, and (e) coherogram between calibrated pressure and corrected vertical acceleration, with (f) its average values. Vertical dashed lines indicate the frequency limits of the compliance band. In panel (f) shaded areas highlight selected windows with higher coherence than the coherence threshold, represented by a vertical dashed line, set at 0.8.

is dominant and  $a_e$  is negligible, but  $a_w$  can increase the measured compliance by up to 5 per cent at the lowest frequencies. To avoid underestimating deep velocities, the effect of  $a_w$  must therefore be removed from the acceleration signal before measuring compliance (Crawford *et al.* 1998). We use eq. (11) to calculate  $a_w$  on the basis of the measured pressure signal (Crawford *et al.* 1998; Zha & Webb 2016), then we subtract it from  $a_d$ .

$$a_w = 2\pi G \rho_w h_w e^{-\kappa H} \quad (11)$$

where  $G \approx 6.6732 \times 10^{-11} \text{ Nm}^2 \text{ kg}^{-2}$  is the gravitational constant of Earth,  $\rho_w \approx 1040 \text{ kgm}^{-3}$  is the water density,  $\kappa(\omega)$  is the ocean infragravity wavenumber,  $H$  the ocean depth, and  $h_w$  represents the sea surface displacement determined from the pressure signal.

## 4.2 Compliance measurement

We calculate compliance using 35-min time windows. We established criteria to select the optimal time windows for calculating the compliance function. In order to minimize bias errors, we choose windows that demonstrate a median coherence greater than 0.8 between pressure and processed vertical component in the compliance frequency band. To filter out windows with anomalous spectra, we also established two conditions based on the amplitude of the PSD. These conditions dictate that, in the compliance frequency band, the pressure PSD should fall between 10 and 50 dB (in units of  $[\text{Pa}^2/\text{Hz}]$ ) and the PSD of vertical component in acceleration should be within the range of  $-170$  to  $-150$  dB (in units of  $[(\text{m/s}^2)^2/\text{Hz}]$ ).

Fig. 6 presents, for station RR52, the spectrogram of calibrated pressure data, the processed vertical acceleration, the coherogram between the two, and the average values of each in the compliance frequency band.

The coherogram exhibits periodic behaviour in the compliance frequency band, with an approximately 3.5-d cycle (Fig. 6f). This pattern suggests a potential correlation with lunar phases, waxing and waning, indicating that the Moon's gravitational tidal forces notably influence compliance measurement.

Coherence is generally maximum when the vertical acceleration is at its minimum, indicating a direct correlation between these two parameters, although there are also cases of high coherence when the vertical acceleration is at its maximum. The high concentration of selected windows when the vertical acceleration is at its minimum probably occurs because there is less noise, allowing the compliance component to be more apparent.

After identifying the optimal windows, we calculated compliance using eq. (6). Fig. 7 shows PSDs, coherence and compliance for each window (PSDs, coherence and compliance measurement). We use the coherence function between the vertical acceleration and pressure for the selected time windows (Fig. 7c) to define the frequency limits of the compliance measurement: here, we use the range in which the mean coherence exceeds a threshold value of 0.8 (vertical dashed black lines). While the theoretical formula from Crawford *et al.* (1991) provides a range for the maximum cut-off frequency of infragravity wave-induced seafloor pressure, the coherence function helps determine the precise frequency limits, typically at the upper end of this range. We set threshold values based on the goal of obtaining at least 500 time windows per station to ensure statistically significant results. At stations with lower data quality, a threshold of 0.8 allowed us to meet this target by including a sufficient number of data points, despite some noise. For higher-quality stations, we used a 0.9 threshold, enhancing data integrity while still achieving the required 500 windows.

## 4.3 Shear velocity inversion using the Metropolis–Hastings method

In this study, we invert the measured compliance to estimate the  $V_s$  model of the ocean bottom subsurface using the Metropolis–Hastings method, a robust nonlinear Bayesian inversion technique (Mosegaard & Tarantola 1995). This approach is not influenced by initial model assumptions and effectively handles the non-convex nature of seismic inversion problems (Zha & Webb 2016). The inversion is executed by perturbing a previous model

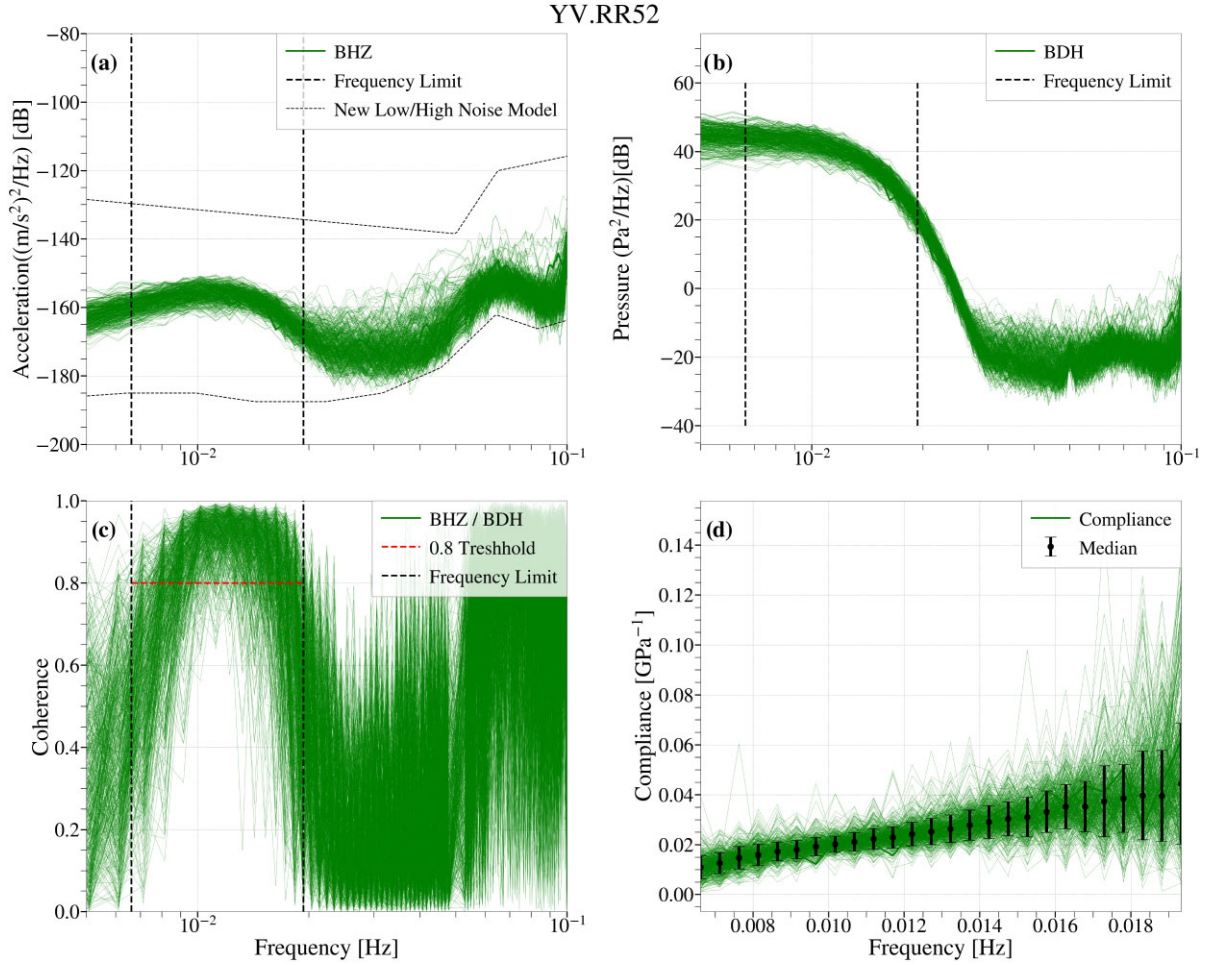


**Figure 7.** Selected time windows from station RR52, illustrating the PSD of seismic data with corrected vertical acceleration (a), PSDs of corrected pressure data (b), the coherence function between vertical acceleration and pressure (c), and the final compliance measurement with error bars (d). Vertical dashed lines indicate the frequency limits of the compliance measurement, while the horizontal dashed line denotes the coherence threshold at 0.8. Each thin solid line corresponds to 35 min of data, showcasing detailed intervals within the data set.

$m_{i-1}$  to propose a new model  $m_i$ , with acceptance based on the likelihood function  $L(m)$  which combines the misfit function  $\chi^2(m) = \frac{1}{N} \sqrt{\sum_{i=1}^N \left( \frac{\eta_i^{\text{obs}} - \eta_i^{\text{pred}}}{\epsilon} \right)^2}$ , where  $N$  is the number of data, and a roughness measure  $R(M)$  (Mosegaard & Tarantola 1995).

The likelihood function,  $L(m)$ , is described as:

$$L(m) = \exp\left(-\frac{1}{2}[\chi^2(m) + \alpha R(m)]\right) \quad (12)$$

where  $\alpha$  is a Lagrange multiplier adjusting the weight of the constraints, selected via the L-curve approach to balance smoothness and fit. In our approach, the roughness measure  $R(M)$  is determined by squaring and summing the second-order derivative, usually a Laplacian, of the  $V_s$  model to gauge curvature.

The probability of accepting the new model is:

$$P_a = \begin{cases} 1 & \text{if } L(m_i) \leq L(m_{i-1}) \\ \exp\left(\frac{L(m_i) - L(m_{i-1})}{\epsilon}\right) & \text{otherwise} \end{cases} \quad (13)$$

We propose new models by randomly perturbing either the  $V_s$  or the thickness of a random layer. During the inversion process, the density and compressional velocity (prescribed from the CRUST1.0 model) are kept constant, as compliance is primarily sensitive to the

shear modulus. Consequently, variations in these parameters do not influence the shape or amplitude of the compliance function.

Model parametrization involves adjusting hyperparameters like  $\alpha$ ,  $V_s$  step size and layer thickness step size to optimize the model while preventing overfitting. The parameters are determined through a grid search aiming for an acceptance rate of 70 to 90 per cent, ensuring efficient convergence (Goffin 1977; Roberts *et al.* 1997). Uncertainties in the compliance measurement, such as noise introduced during the recording and the post-correction, coherence thresholds, and calibration variability, are incorporated into the inversion through the likelihood function in the Metropolis–Hastings algorithm. These uncertainties are reflected in the variability of the  $V_s$  models, with broader compliance error bars leading to reduced model resolution and confidence intervals, particularly at stations with lower data quality (e.g. RR40). Prior knowledge and the geological context of each station, played a significant role in reducing uncertainties in the resulting shear velocity models by filtering out geophysically implausible results during the inversion process. The model setup includes constraints on the number of layers, Moho discontinuity depth, and permissible shear velocities for each layer, derived from geological knowledge and prior studies (Pasyanos *et al.* 2013). An estimate of the compliance uncertainty,  $\epsilon [|\hat{\eta}(\omega)|]$ , is provided, where  $n_d$  represents the number of data windows used

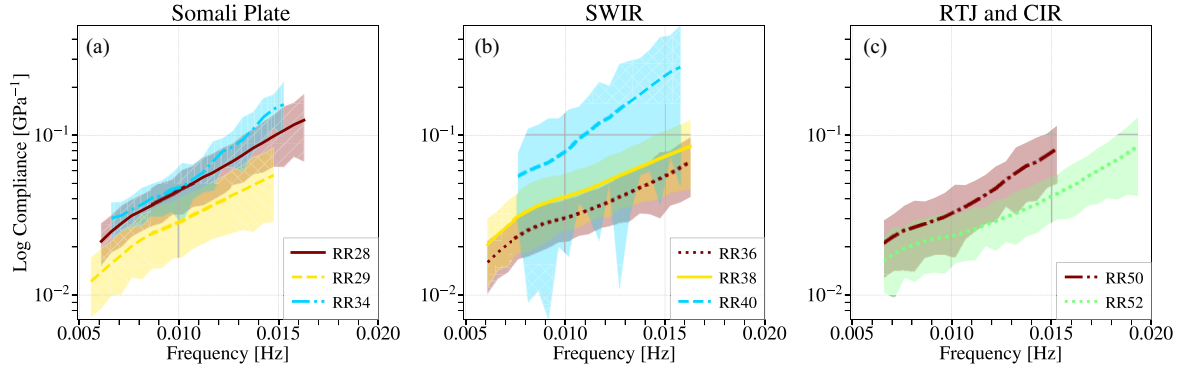


**Figure 8.** Logarithmic plot of normalized compliance functions for various stations. (a) Stations located on the Somali Plate. (b) Stations along the SWIR, including RR40, which suffers from low data quality and limited measurements, leading to greater uncertainty in measurement and adversely affecting the final estimation of the  $V_s$  model. (c) Stations situated on the RTJ and the CIR.

to compute the spectra and coherence (Bendat & Piersol 1993).

$$\epsilon[|\hat{\eta}(\omega)|] = \frac{\sqrt{1 - \hat{\gamma}_{pz}^2(\omega)}}{|\hat{\gamma}_{pz}(\omega)|\sqrt{2n_d}} |\hat{\eta}(\omega)| \quad (14)$$

#### Inversion model parametrization and constraints

The number of layers in our inversion models was determined through an initial exploratory analysis, leveraging the CRUST 1.0 model (Laske *et al.* 2013). We adjusted the number of layers based on station-specific data quality to enhance fit and resolution, employing an adaptive approach that refines the model in heterogeneous regions (Shapiro & Ritzwoller 2002). The inversion process was conducted using models with 3, 6 and 9 layers, plus a half-space. For stations located on sedimentary layers, we tested models with 4, 7 and 10 layers, plus a half-space. In these cases, each non-sedimentary layer from the CRUST1.0 model was subdivided into 2 or 3 layers to increase resolution and accommodate models with a higher number of layers. Our analysis revealed that the models with 6 layers for stations on the crust and 7 layers for stations on sediments provided the best results, based on the evaluation of the misfit function and the distribution of the final  $V_s$  models. We aimed for a Gaussian distribution in the final  $V_s$  models, which served as a desirable outcome to ensure the robustness of the inversion. While our inversion strategy employs a stochastic sampling scheme with adaptive model parameterization, the initial motivation to explore varying layered models draws conceptual inspiration from earlier minimum-structure compliance inversions based on Occam's Inversion (Constable *et al.* 1987), though our inversion method differs fundamentally in being probabilistic rather than deterministic.

Although the initial starting model does not inherently influence the inversion process, we imposed constraints to guide the search space effectively. These constraints were defined as percentage-based boundaries relative to the starting model. For shallow structures, the lower limit was set to  $V_s = 0$ , and the upper limit was +25 per cent of the starting model values. For deeper structures, the boundaries were set to  $V_s = -100$  and +25 per cent of the starting model. This approach ensured that the inversion process was constrained to search within these pre-defined limits, providing realistic and geologically plausible solutions. The thickness of each layer was constrained to be non-negative, meaning that layers were never entirely removed from the process. A layer with zero thickness remained in the model and could be iteratively adjusted, ensuring its influence on the inversion process. Furthermore, the crustal thickness and Moho depth were allowed to vary within a  $\pm 1$

km range, providing flexibility while maintaining realistic geological constraints.

## 5 RESULTS

### 5.1 RHUM-RUM's experiment compliance functions

We present the logarithmic plot of normalized compliance functions for the stations of this study in Fig. 8. Horizontal compliance was not observed at any of the stations in this region based on coherence analysis between horizontal components and pressure gauges. The data quality at RR40 is relatively poor (Fig. 8b), leading to significant uncertainties affecting the reliability of its  $V_s$  results. This compromised data quality limits our ability to confidently interpret the results. Given this, we must consider the possibility that RR40 might not reflect the same processes as other stations, or if it does, that we cannot robustly ascertain it with the current dataset.

Seafloor compliance is sensitive to the shear modulus at depth, which increases with the wavelength of infragravity waves (Crawford *et al.* 1998). A low-velocity anomaly (LVA) typically creates a peak in the compliance function, where the depth of the LVA is inversely related to the peak's frequency (Hulme *et al.* 2005). A shallow LVA results in a broader peak in the compliance function; however, the peaks that are caused by intermediate/deep LVAs may be masked by the effects of shallow structures, such as thick sedimentary layers with intermediate shear velocities. The influence of these sedimentary layers on the compliance function depends on their thickness and shear velocity properties, which can obscure the characteristic signature of the LVA (Willoughby & Edwards 2000; Wang *et al.* 2010). The ascending trend of each compliance measurements confirms the increase in  $V_s$  with depth. Concave segments within the compliance measurement, as observed in Fig. 8, are caused by velocity anomalies beneath the station.

### 5.2 Shear velocity profile

Using the robust inversion methodology detailed above, Fig. 9 synthesizes the estimated  $V_s$  models at all the stations. The variability among the profiles reflects our method's adaptability to the diverse geological conditions at each station, supported by the rigorous statistical framework of the Metropolis–Hastings inversion.

The  $V_s$  profiles at intraplate station RR28 (Fig. 9a) show an extremely low  $V_s$  of  $0.4 \text{ km s}^{-1}$  at the seafloor, which persists down to  $0.5 \text{ km}$  below the seafloor (BSF). Beyond this, a sudden increase to  $2.7 \text{ km s}^{-1}$  is noted, followed by a strong gradient elevating  $V_s$

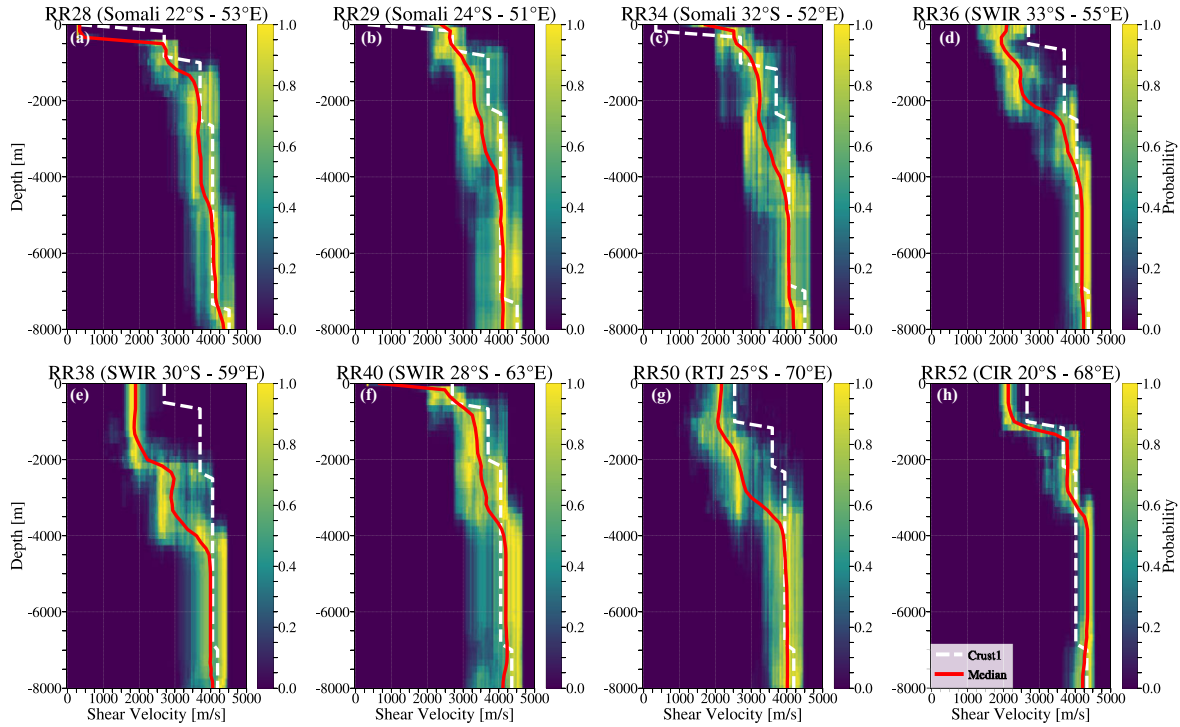


**Figure 9.**  $V_s$  profiles as a function of depth, obtained using the Metropolis-Hastings inversion method of compliance measurements for each station. Solid lines represent the median estimated  $V_s$  model. The colour bars represent the posterior distribution / probability density of  $V_s$  values, with higher probabilities indicated by warmer colours and lower probabilities by cooler colours.

to  $3.5 \text{ km s}^{-1}$  at a depth of 1.2 km BSF. From 1.2 km to about 4.3 km BSF, the profile maintains a near-zero gradient at  $3.5 \text{ km s}^{-1}$ . Subsequent depths up to 7.5 km BSF reveal a steady increment to  $4 \text{ km s}^{-1}$ , followed by a final surge to  $4.2 \text{ km s}^{-1}$  at the maximum depth resolved by the inversion.

The  $V_s$  profiles at stations RR29 and RR34 (Figs 9b and c) exhibit similar behaviours with variations in depth and gradient intensities. At station RR29 (Fig. 9b), the  $V_s$  profile starts at  $2 \text{ km s}^{-1}$  at the seafloor and shows a low gradient increase to  $4 \text{ km s}^{-1}$  by 4 km BSF, then remains constant at this velocity up to the maximum depth resolved by the inversion. In contrast, at station RR34 (Fig. 9c), the  $V_s$  profile begins with a rapid velocity increase from less than  $1 \text{ km s}^{-1}$  at the seafloor to  $3.5 \text{ km s}^{-1}$  by 1 km BSF. This is followed by a gradual increase to  $4 \text{ km s}^{-1}$  by about 3 km BSF, which then remains steady until a depth of 7.5 km BSF, where there is a notable jump to  $4.2 \text{ km s}^{-1}$ , sustained up to the maximum depth of the inversion.

The  $V_s$  profiles at two of the SWIR stations (RR36 and RR38) and at the RTJ (RR50) are similar (Figs 9d, e and g): a low (RR36 and RR50) to zero (RR38) gradient in the upper crust with very low  $V_s$  ( $2\text{--}2.4 \text{ km s}^{-1}$ ) down to approximately 2 km BSF, followed by a higher gradient down to 4–4.3 km BSF and  $V_s$  values of 4 to  $4.2 \text{ km s}^{-1}$  that remain constant down to the maximum depth resolved by the inversion, approximately 8 km. The  $V_s$  profile at the CIR station (RR52; Fig. 9h) is faster, featuring a 1 km-thick upper crustal lower velocity layer ( $V_s = 2.1 \text{ km s}^{-1}$ ), then a strong gradient to  $3.8 \text{ km s}^{-1}$  at 1.5 km BSF, a near zero gradient down to 3 km BSF, and another strong gradient to  $4.25 \text{ km s}^{-1}$  at 3.5 km BSF. Station RR40 at the SWIR, which has the lowest data quality (Fig. 9f), yielded the slowest near-seafloor  $S$ -wave velocities but also the fastest overall  $V_s$  model (Fig. 9f): a strong upper crustal gradient from  $<1 \text{ km s}^{-1}$  at the seafloor to  $3.4 \text{ km s}^{-1}$  at 1 km BSF, then a low gradient to

$3.5 \text{ km s}^{-1}$  at 3.5 km BSF, and another strong gradient to 4–4.1  $\text{km s}^{-1}$  at 4 km BSF.

Fig. S6 (Supporting Information) illustrates the sensitivity of the compliance function in resolving the depth and thickness of LVAs and the depth of the Moho, providing robust and reliable insights into these key crustal features.

## 6 DISCUSSION

Our study investigates a geologically intricate region marked by the intersection of three tectonic plates: the Somali Plate, the Australian Plate and the Antarctic Plate. Specifically, stations RR28, RR29 and RR34 are situated on the normal oceanic crust of the Somali Plate. The crust at RR28 and RR29 was formed by the CIR, while the crust at RR34 originated from the SWIR. This complex area also features two significant mid-oceanic ridges: the SWIR, with stations RR36, RR38 and RR40 located on its ultraslow spreading segment, and the CIR, home to station RR52. The SWIR exhibits unique morphological and geological characteristics (Sauter & Cannat 2010; Dick *et al.* 2019), such as a rugged seafloor, large fault blocks, deep rift valleys, and the common exposure of mantle-derived peridotites, which are emplaced into the crust by large offset normal faults.

Station RR50 is located at the RTJ, where the SWIR, CIR, and SEIR intersect, creating a complex geodynamic setting at a ridge-ridge boundary shaped by the interaction of three diverging tectonic plates.

Intraplate observations from the stations on the Somali Plate (RR28, RR29 and RR34 on Fig. 1) reveal notable variations in shallow  $V_s$ , as depicted in Fig. 10a). These variations in  $V_s$  correlate with differences in the thickness of the sedimentary layers, which may be influenced by sediment transport processes originating from

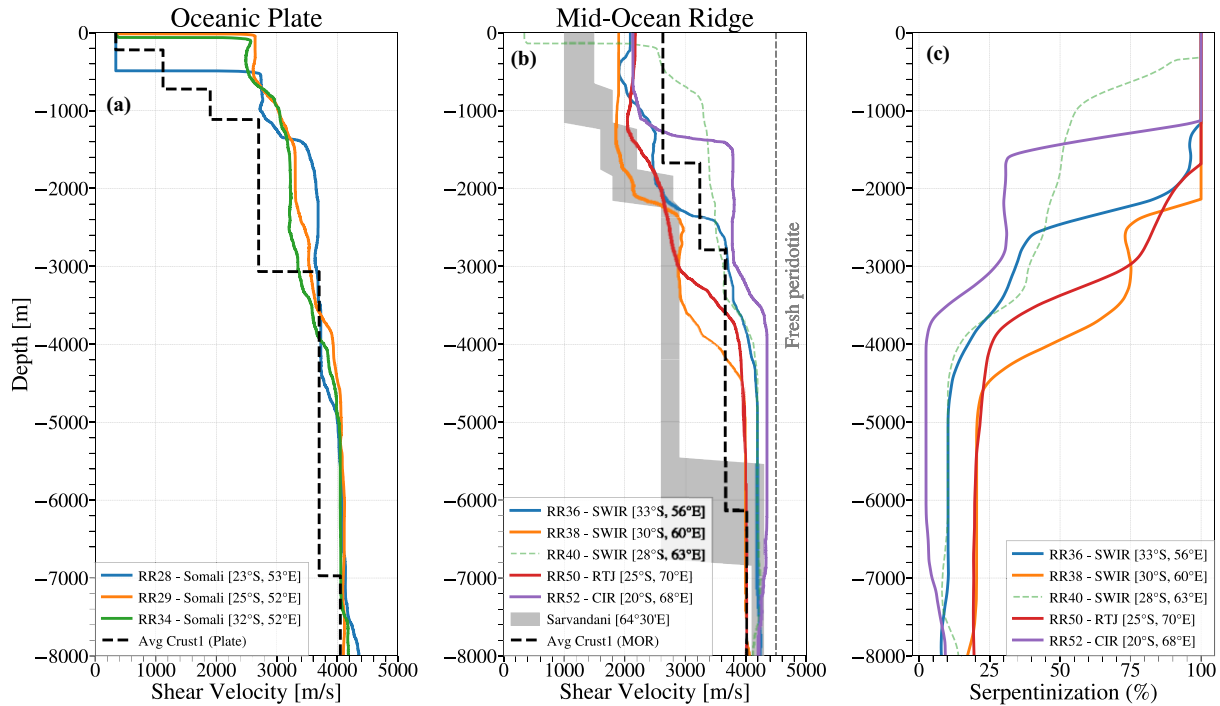


**Figure 10.**  $V_s$  profiles for: (a) Intraplate stations, where the black dashed line represents the  $V_s$  from the CRUST1 model (average model for intraplate stations) in the Somali Plate; (b) mid-oceanic ridge stations, with the dashed line indicating the  $V_s$  from the CRUST1 model (average model for stations on the SWIR and CIR). The shaded area represents the range of  $V_s$  values from a seismic noise study by Sarvandani *et al.* (2021) at the SWIR,  $64^\circ 30' E$ ; (c) serpentinization percentage calculated at mid ocean ridge stations, assuming a fully ultramafic crustal layer where low  $V_s$  values are solely due to serpentinization. This is based on a linear empirical relation from, using velocities of  $4.2 \text{ km s}^{-1}$  for 0 per cent serpentinization and  $2.2 \text{ km s}^{-1}$  for 100 per cent serpentinization.

La Réunion Island (Sisavath *et al.* 2012; Babonneau *et al.* 2013, 2016), whose impact on the thickness and  $V_s$  of the oceanic crust's sedimentary layers diminishes with increased distance from the island (Laske *et al.* 2013; Straume *et al.* 2019).

Furthermore, At RR29 and RR34, higher sedimentary shear velocities compare to RR28 (Fig. 10a) suggest a more consolidated sediment layer, whereas the lower sedimentary  $V_s$  at RR28 could suggest an unconsolidated sediment layer. However, other factors, such as lithology, pore fluid content, and burial history, may also contribute to these variations. This distinction is influenced by the proximity to La Réunion Island and the degree of consolidation and composition of the sediment layers.

Station RR34 exhibits a potential LVA at depths ranging from approximately 2 to 3.5 km, as illustrated in Fig. 9(c). Despite this anomaly, the overall average  $V_s$  at RR34 is comparable to that observed at RR29, suggesting similar crustal structures, as detailed in Fig. 10(a). Importantly, these findings confirm the CRUST1 model but with enhanced resolution in the upper crust. Our result reveal a pronounced  $V_s$  gradient in layer 2, which contrasts starkly with the relatively small gradient observed in layer 3. This observation is critical as it underscores a distinct transition between these layers at approximately 3 km BSF across the three stations. Such high-resolution intraplate result not only corroborate but also refine the layered model proposed by CRUST1, highlighting our ability to capture subtle yet significant structural variations within the crust that were previously unresolved.

Stations on SWIR and CIR exhibit significant shallow LVAs extending down to 3 km beneath the seafloor, as shown in Fig. 10(b). These anomalies are most likely associated with processes such as serpentinization, magmatism and varying porosity within the oceanic crust, triggered by the specific tectonic and thermal regimes

of these spreading centres (e.g. Miller & Christensen 1997; Cannat *et al.* 2006; Searle 2013).

The 3 SWIR stations (RR36, RR38 and RR40) are located in oblique sections of the ridge (Fig. S2, Supporting Information), featuring deep axial valleys and a crust that is likely extensively faulted and composed significantly of variably serpentinized peridotite (Dick *et al.* 2003, 2019; Cannat *et al.* 2006). This may also be the case in the deep axial valley at the RTJ (RR50), where oceanic crust, formed at the intermediate-spreading the CIR and SEIR, is rifted by the ultraslow SWIR. With the exception of RR40, which has significantly lower quality data and therefore a less reliable  $V_s$  model (Fig. 8f),  $V_s$  profiles at these locations are indeed similar and significantly slower than the Crust 1 model predicts for these locations (Fig. 9). The most likely explanation for these lower velocities is that the upper 4 km of the oceanic lithosphere at these stations comprises a significant proportion of serpentinized peridotites and is more tectonized than the fully magmatic (composed of solidified melt from the mantle, typically basaltic in composition) CRUST1 reference model. This interpretation is consistent with studies from other locations along the same ridge, where similar serpentinization and tectonization patterns have been observed (e.g. Rouméjon & Cannat 2014; Rouméjon *et al.* 2015; Karpoff *et al.* 2017).  $P$  and  $S$  wave velocities in peridotites decrease linearly with the degree of serpentinization (from  $V_s$   $4.2\text{--}4.35 \text{ km s}^{-1}$  in pristine peridotites to  $V_s$   $2.1\text{--}2.3 \text{ km s}^{-1}$  in fully serpentinized peridotites (Miller & Christensen 1997). The very low  $V_s$  ( $2\text{--}2.4 \text{ km s}^{-1}$ ) modelled in the upper 2 km BSF could therefore indicate near 100 per cent serpentinization, which is often associated with increased fracture porosity, though the extent of this porosity may vary. The higher  $V_s$  gradient between 2 and 4 km BSF could then be interpreted as a progressive decrease in the degree of serpentinization down to

pristine or near-pristine mantle (Fig. 10c). This interpretation was proposed by Sarvandani *et al.* (2021) to explain similarly low crustal  $V_s$  values revealed by ambient seismic noise tomography/imaging at  $64^{\circ}30'E$  at the SWIR.

The faster-spreading CIR at station RR52 features more subdued relief, and available ship bathymetry (Fig. S2, Supporting Information) indicates regularly spaced abyssal hills typical of ridges with a fully or nearly fully magmatic crust (Sauter *et al.* 2011). The  $V_s$  profile at this station is close to the fully magmatic and little tectonized CRUST1 model (Fig. 9h), except in the uppermost 1 km of the crust, which has very low  $V_s$  ( $2.1 \text{ km s}^{-1}$ ). We propose that these low uppermost crust  $V_s$  values are due to porosity (from fractures and voids in and between piled lava flows). The  $V_s$  profile obtained here for nearby station RR40 (SWIR  $63.3^{\circ}E$ ) is, by contrast, very similar to the predicted fully magmatic and little tectonized CRUST1 model (Fig. 9f), yet the geological setting of this station, in an oblique, deep axial valley section of the ridge (Fig. S2, Supporting Information), suggests extensive faulting and variably serpentinized peridotites in the crust.

It is difficult, if not impossible, to distinguish between heat/magmatization and serpentinization as the source of low velocities based on single, isolated measurements, although it seems more likely that serpentinization would be responsible for LVAs that extend up to the seafloor. These stations were located to optimize a large-scale tomographic survey, not to study mid-ocean ridge dynamics. They serve, however, as a first look at the fascinating  $V_s$  structure on and near the SWIR and CIR axes, as well as at the RTJ, and they indicate that temporary local networks of compliance measurements could significantly contribute to our knowledge of the magmatism and serpentinization of these accretionary features.

## 7 CONCLUSION

This study represents the first constraints on subsurface  $V_s$  structures in the Indian Ocean through compliance function analysis. Our rigorous data processing methodology minimizes noise and optimizes window selection for compliance measurement, including dynamic tilt effect correction on an hourly basis and documenting the post-deployment settling of stations. We present a specialized software, named ‘ComPy,’ designed to automate the processing steps required for this study, enhancing efficiency and accuracy in seafloor compliance analysis.

The inversion of the compliance function using the Metropolis–Hastings method allows for precise modeling of shear velocities, adeptly handling the non-convex nature of seismic data and variability across stations. Our study leverages data from eight BBOBS from the RHUM-RUM experiment conducted in 2012. The resulting  $V_s$  models, reaching depths of up to 8 km, highlight significant variations in  $V_s$  anomalies, particularly in regions associated with intraplate settings and ultraslow to intermediate spreading ridges. Intraplate shallow  $V_s$  profiles reflect the presence of sedimentary layers with varying degrees of consolidation. Conversely, anomalies at mid-ocean ridges likely indicate the presence of serpentinized peridotites and other lithological variations. These findings are essential for understanding the geodynamic processes occurring at mid-ocean ridges.

## ACKNOWLEDGMENTS

This research was part of the SPIN project, an Innovative Training Network (ITN) funded by the European Commission under

the Horizon 2020 Marie Skłodowska-Curie Action (MSCA), grant agreement no. 955515.

## SUPPORTING INFORMATION

Supplementary data are available at *GJIRAS* online.

### Supplementary figures

Please note: Oxford University Press is not responsible for the content or functionality of any supporting materials supplied by the authors. Any queries (other than missing material) should be directed to the corresponding author for the paper.

## DATA AVAILABILITY

The data used in this study are part of the ‘‘YV’’ network available through the RESIF data centre website at <https://doi.org/10.15778/RESIF.YV2011>. The data set includes broad-band ocean-bottom seismometer data from the RHUM-RUM experiment. Access to the data is subject to the data-sharing policies of RESIF.

The *ComPy* software package, developed for the advanced processing and analysis of ocean-bottom seismological data, is available at <https://github.com/MohammadAmin-Aminian/ComPy> and is archived with the DOI: [10.5281/zenodo.13380107](https://doi.org/10.5281/zenodo.13380107). *ComPy* facilitates robust calculations and inversions of compliance measurements, enabling precise mapping of subsurface shear velocity structures. This software is provided for non-commercial use, and full documentation is available in the repository.

## REFERENCES

- Babonneau, N. *et al.*, 2013. Direct sediment transfer from land to deep-sea: Insights into shallow multibeam bathymetry at La Réunion Island, *Mar. Geol.*, **346**, 47–57.
- Babonneau, N., Villeneuve, N., Mazuel, A. & Bachèlery, P., 2016. Erosion and volcanoclastic sedimentation at piton de la fournaise: from source to deep marine environment, in *Active Volcanoes of the World*, pp.71–90, eds, Bachèlery, P., Lénat, J.-F., Di Muro, A. & Michon, L., Springer-Verlag, Berlin/Heidelberg, Germany.
- Barruol, G. & Sigloch, K., 2013. Investigating La Réunion Hot Spot From Crust to Core, *EOS Trans. Am. Geophys. Un.*, **94**(23), 205–207.
- Bell, S.W., Forsyth, D.W. & Ruan, Y., 2015. Removing noise from the vertical component records of ocean-bottom seismometers: Results from year one of the cascadia initiative, *Bull. seism. Soc. Am.*, **105**(1), 300–313.
- Bendat, J.S. & Piersol, A.G., 1993. *Engineering Applications of Correlation and Spectral Analysis*, pp. 458, Wiley, New York.
- Bertin, X. *et al.*, 2018. Infragravity waves: from driving mechanisms to impacts, *Earth-Sci. Rev.*, **177**, 774–799.
- Bradner, H., 1963. Probing sea-bottom sediments with microseismic noise, *J. geophys. Res.*, **68**(6), 1788–1791.
- Cannat, M., Rommevaux-Jestin, C., Sauter, D., Deplus, C. & Mendel, V., 1999. Formation of the axial relief at the very slow spreading Southwest Indian Ridge ( $49^{\circ}$  to  $69^{\circ}E$ ), *J. Geophys. Res. Solid Earth*, **104**(B10), 22 825–22 843.
- Cannat, M., Sauter, D., Mendel, V., Ruellan, E., Okino, K., Escartin, J., Combier, V. & Baala, M., 2006. Modes of seafloor generation at a melt-poor ultraslow-spreading ridge, *Geology*, **34**(7), 605–608.
- Constable, S.C., Parker, R.L. & Constable, C.G., 1987. Occam’s inversion: a practical algorithm for generating smooth models from electromagnetic sounding data, *Geophysics*, **52**(3).
- Cox, C., Deaton, T. & Webb, S., 1984. A Deep-Sea Differential Pressure Gauge, *J. Atmos. Ocean. Technol.*, **1**, 237–246.
- Crawford, W.C., 2004. The sensitivity of seafloor compliance measurements to sub-basalt sediments, *J. geophys. Int.*, **157**(3), 1130–1145.

- Crawford, W.C. & Singh, S.C., 2008. Sediment shear properties from seafloor compliance measurements: Faroes-Shetland basin case study, *Geophys. Prospect.*, **56**(3), 313–325.
- Crawford, W.C. & Webb, S.C., 2000. Identifying and removing tilt noise from low-frequency (<0.1 Hz) seafloor vertical seismic data, *Bull. seism. Soc. Am.*, **90**(4), 952–963.
- Crawford, W.C. & Webb, S.C., 2002. Variations in the distribution of magma in the lower crust and at the Moho beneath the East Pacific Rise at 9°–10°N, *Earth planet. Sci. Lett.*, **203**(1), 117–130.
- Crawford, W.C., Webb, S.C. & Hildebrand, J.A., 1991. Seafloor compliance observed by long-period pressure and displacement measurements, *J. geophys. Res.*, **96**(B10).
- Crawford, W.C., Webb, S.C. & Hildebrand, J.A., 1998. Estimating shear velocities in the oceanic crust from compliance measurements by two-dimensional finite difference modeling, *J. Geophys. Res. Solid Earth*, **103**(5), 9895–9916.
- Deen, M., Wielandt, E., Stutzmann, E., Crawford, W., Barruol, G. & Sigloch, K., 2017. First observation of the Earth's permanent free oscillations on Ocean Bottom Seismometers, *Geophys. Res. Lett.*, **44**(10), 10988–10996.
- Dick, H.J., Lin, J. & Schouten, H., 2003. An ultraslow-spreading class of ocean ridge, *Nature*, **426**(6965), 405–412.
- Dick, H.J., Kvassnes, A.J., Robinson, P.T., MacLeod, C.J. & Kinoshita, H., 2019. The Atlantis Bank Gabbro Massif, Southwest Indian Ridge, *Prog. Earth Planet. Sci.*, **6**(1), 1–70.
- DJ, Miller, & Christensen, N.I., 1997. Seismic velocities of lower crustal and upper mantle rocks from the slow-spreading mid-atlantic ridge, South of the Kane transform zone, in *Proceeding of the Ocean Drilling Program, Scientific Results*, pp. 437–454, eds, Karson, J.A., Cannat, M., Miller, D.J. & Elthon, D., Ocean Drilling Program, College Station, Texas.
- Doran, A.K. & Crawford, W.C., 2020. Continuous evolution of oceanic crustal structure following an eruption at Axial Seamount, Juan de Fuca Ridge, *Geology*, **48**(5), 452–456.
- Doran, A.K. & Laske, G., 2016. Infragravity waves and horizontal seafloor compliance, *J. Geophys. Res. Solid Earth*, **121**(1), 260–278.
- Doran, A.K., Rapa, M., Laske, G., Babcock, J. & McPeak, S., 2019. Calibration of differential pressure gauges through *In Situ* testing, *Earth Space Sci.*, **6**(12), 2663–2670.
- Drobia, R.K., Ghose, I., Subramanyam, A.S., Malleswara Rao, M.M., Kessarkar, P. & Murthy, K.S., 2000. Magnetic and bathymetric investigations over the Vema Region of the Central Indian Ridge: tectonic implications, *Mar. Geol.*, **167**(3–4), 413–423.
- Goffin, J.L., 1977. On convergence rates of subgradient optimization methods, *Math. Prog.*, **13**(1), 329–347.
- Gomberg, J.S. & Masters, T.G., 1988. Waveform modelling using locked-mode synthetic and differential seismograms: application to determination of the structure of Mexico, *J. geophys. Int.*, **94**(2), 193–218.
- Harmon, N., Laske, G., Crawford, W. & Rychert, C., 2022. Tilt Corrections for Normal Mode Observations on Ocean Bottom Seismic Data, an example from the PI-LAB experiment, *Seismica*, **1**(1).
- Herbers, T., Elgar, S., Guza, R. & O'Reilly, W., 1994. Infragravity-frequency (0.005–0.05 Hz) motions on the shelf. Part I: forced waves, *J. Phys. Oceanogr.*, **24**(5), 917–927.
- Hulme, T., Ricolleau, A., Bazin, S., Crawford, W.C. & Singh, S.C., 2003. Shear wave structure from joint analysis of seismic and seafloor compliance data, *J. geophys. Int.*, **155**(2), 514–520.
- Hulme, T., Crawford, W.C. & Singh, S.C., 2005. The sensitivity of seafloor compliance to two-dimensional low-velocity anomalies, *J. geophys. Int.*, **163**(2), 547–558.
- Janiszewski, H.A., Gaherty, J.B., Abers, G.A., Gao, H. & Eilon, Z.C., 2019. Amphibious surface-wave phase-velocity measurements of the Cascadia subduction zone, *J. geophys. Int.*, **217**(3), 1929–1948.
- Kamesh Raju, K.A., Samudrala, K., Drobia, R.K., Amarnath, D., Ramachandran, R. & Mudholkar, A., 2012. Segmentation and morphology of the Central Indian Ridge between 3°S and 11°S, Indian Ocean, *Tectonophysics*, **554–557**, 114–126.
- Karpoff, A., Sauter, D., Cannat, M., Ulrich, M. & Manatschal, G., 2017. Fe-Si Oxides Tracing the Ongoing Low-T° Hydrothermal Alteration of Exhumed Serpentinites at the Ultraslow-spreading Southwest Indian Ridge, *Procedia Earth Planet. Sci.*, **17**, 280–283.
- Kennett, B.L.N.B.L.N., 2009. *Seismic Wave Propagation in Stratified Media*, ANU E Press.
- Krishna, M.R., 1996. Isostatic response of the Central Indian Ridge (Western Indian Ocean) based on transfer function analysis of gravity and bathymetry data, *Tectonophysics*, **257**(2–4 SPEC. ISS.), 137–148.
- Kuo, B.Y., Crawford, W.C., Webb, S.C., Lin, C.R., Yu, T.C. & Chen, L., 2015. Faulting and hydration of the upper crust of the SW Okinawa Trough during continental rifting: evidence from seafloor compliance inversion, *Geophys. Res. Lett.*, **42**(12), 4809–4815.
- Laske, G., Masters, G., Ma, Z. & Pasyanos, M., 2013. laske-egu13-crust1, *EGU General Assembly*, **15**.
- Mosegaard, K. & Tarantola, A., 1995. Monte Carlo sampling of solutions to inverse problems, *J. geophys. Res.*, **100**(B7). doi:10.1029/94JB03097
- Mosher, S.G., Audet, P. & Gosselin, J.M., 2021a. Shear-Wave Velocity Structure of Sediments on Cascadia's Continental Margin From Probabilistic Inversion of Seafloor Compliance Data, *Geochem. Geophys. Geosyst.*, **22**(9).
- Mosher, S.G., Eilon, Z., Janiszewski, H. & Audet, P., 2021b. Probabilistic inversion of seafloor compliance for oceanic crustal shear velocity structure using mixture density neural networks, *J. geophys. Int.*, **227**(3), 1879–1892.
- Müller, R.D., Sdrolias, M., Gaina, C. & Roest, W.R., 2008. Age, spreading rates, and spreading asymmetry of the world's ocean crust, *Geochem. Geophys. Geosyst.*, **9**(4). doi:10.1029/2007GC001743
- Pasyanos, M.E. et al., 2013. Update on CRUST1.0 - A 1-degree Global Model of Earth's Crust, *EGUGA*, **15**, 2013–2658.
- Patriat, P. & Segoufin, J., 1988. Reconstruction of the Central Indian Ocean, *Tectonophysics*, **155**(1–4), 211–234.
- Rawat, A., Arduhin, F., Ballu, V., Crawford, W., Corela, C. & Aucan, J., 2014. Infragravity waves across the oceans, *Geophys. Res. Lett.*, **41**(22), 7957–7963.
- Rebeyrol, S., Ker, S., Duval, L. & Crawford, W.C., 2024. Revisiting the OBS seafloor compliance signal removal with a stationarity and stacking-based approach: the BRUIT-FM toolbox, *J. geophys. Int.*, **239**(1), 386–401.
- Roberts, G.O., Gelman, A. & Gilks, W.R., 1997. Weak convergence and optimal scaling of random walk Metropolis algorithms, *Ann. Appl. Probability*, **7**(1), 110–120.
- Roumèjon, S. & Cannat, M., 2014. Serpentinization of mantle-derived peridotites at mid-ocean ridges: mesh texture development in the context of tectonic exhumation, *Geochem. Geophys. Geosyst.*, **15**(6), 2354–2379.
- Roumèjon, S., Cannat, M., Agrinier, P., Godard, M. & Andreani, M., 2015. Serpentinization and fluid pathways in tectonically exhumed peridotites from the Southwest Indian Ridge (62–65°E), *J. Petrol.*, **56**(4), 703–734.
- Ruan, Y., Forsyth, D.W. & Bell, S.W., 2014. Marine sediment shear velocity structure from the ratio of displacement to pressure of Rayleigh waves at seafloor, *J. Geophys. Res. Solid Earth*, **119**(8), 6357–6371.
- Sarvandani, M.M., Kästle, E., Boschi, L., Leroy, S. & Cannat, M., 2021. Seismic ambient noise imaging of a Quasi-amagmatic ultra-slow spreading ridge, *Remote Sens.*, **13**(14).
- Sauter, D. & Cannat, M., 2010. The Ultraslow Spreading Southwest Indian Ridge, *Diversity of Hydrothermal Systems on Slow Spreading Ocean Ridges Geophysical Monograph Series*, American Geophysical Union, Washington, D.C. **Vol. 188**.
- Sauter, D., Sloan, H., Cannat, M., Goff, J., Patriat, P., Schaming, M. & Roest, W.R., 2011. From slow to ultra-slow: How does spreading rate affect seafloor roughness and crustal thickness?, *Geology*, **39**(10), 911–914.
- Searle, R., 2013. Mid-ocean ridges, pp. 1–351, ed. Gibbons, B. & Angela, S., Cambridge University Press, Cambridge, UK & New York, USA. doi:10.1017/CBO9781139084260
- Shapiro, N.M. & Ritzwoller, M.H., 2002. Monte-Carlo inversion for a global shear-velocity model of the crust and upper mantle, *J. geophys. Int.*, **151**(1), 88–105.

- Sisavath, E. *et al.*, 2012. Processes controlling a volcanoclastic turbiditic system during the last climatic cycle: example of the Cilaos deep-sea fan, offshore La Réunion Island, *Sedimentary Geology*, **281**, 180–193.
- Sorrells, G.G. & Goforth, T.T., 1973. Low-frequency earth motion generated by slowly propagating partially organized pressure fields, *Bull. seism. Soc. Am.*, **63**(5), 1583–1601.
- Stähler, S.C. *et al.*, 2016. Performance report of the RHUM–RUM ocean bottom seismometer network around La Réunion *Adv. Geosci.*, **41**, 43–63.
- Straume, E.O. *et al.*, 2019. GlobSed: updated total sediment thickness in the World's oceans, *Geochem. Geophys. Geosyst.*, **20**(4), 1756–1772.
- Tian, Y. & Ritzwoller, M.H., 2017. Improving ambient noise cross-correlations in the noisy ocean bottom environment of the Juan de Fuca plate, *J. geophys. Int.*, **210**(3), 1787–1805.
- Tolstoy, M., Constable, S., Orcutt, J., Staudigel, H., Wyatt, F.K. & Anderson, G., 1998. Short and long baseline tiltmeter measurements on axial seamount, Juan de Fuca Ridge, *Phys. Earth planet. Inter.*, **108**(2), 129–141.
- Wang, J.H., Chi, W.C., Edwards, R.N. & Willoughby, E.C., 2010. Effects of sea states on seafloor compliance studies, *Mar. Geophys. Res.*, **31**(1), 99–107.
- Webb, S.C. & Crawford, W.C., 1999. Long period seafloor seismology and deformation under ocean waves, *Bull. seism. Soc. Am.*, **89**(6), 1535–1542.
- Welch, P.D., 1967. The use of fast Fourier transform for the estimation of power spectra: a method based on time averaging over short, modified periodograms., *IEEE Transactions on Audio and Electroacoustics*, **15**(2).
- Willoughby, E.C. & Edwards, R.N., 1997. On the resource evaluation of marine gas-hydrate deposits using seafloor compliance methods, *J. geophys. Int.*, **131**(3), 751–766.
- Willoughby, E.C. & Edwards, R.N., 2000. Shear velocities in Cascadia from seafloor compliance measurements, *Geophys. Res. Lett.*, **27**(7), 1021–1024.
- Withers, M., Aster, R., Young, C., Beiriger, J., Harris, M., Moore, S. & Trujillo, J., 1998. A comparison of select trigger algorithms for automated global seismic phase and event detection, *Bull. seism. Soc. Am.*, **88**(1), 95–106.
- Yamamoto, T. & Torii, T., 1986. Seabed shear modulus profile inversion using surface gravity (water) wave induced bottom motion, *Geophys. J. R. Astron. Soc.*, **85**(2), 413–431.
- Zha, Y. & Webb, S.C., 2016. Crustal shear velocity structure in the Southern Lau Basin constrained by seafloor compliance, *J. Geophys. Res. Solid Earth*, **121**(5), 3220–3237.
- Zhu, W. & Beroza, G.C., 2019. PhaseNet: A Deep-Neural-Network-Based Seismic Arrival Time Picking Method, *J. geophys. Int.*, **216**(1), 261–273.